

Received July 15, 2019, accepted September 3, 2019, date of publication September 6, 2019, date of current version September 20, 2019.

Digital Object Identifier 10.1109/ACCESS.2019.2939798

Organic Multi-Channel Optoelectronic Sensors for Wearable Health Monitoring

YASSER KHAN¹, DONGGEON HAN¹, JONATHAN TING¹, MARUF AHMED¹,
RAMUNE NAGISSETTY², AND ANA C. ARIAS¹

¹Department of Electrical Engineering and Computer Sciences, University of California, Berkeley, CA 94720, USA

²Intel Labs, Hillsboro, OR 97006, USA

Corresponding authors: Yasser Khan (yasser.khan@berkeley.edu) and Ana C. Arias (acarias@eecs.berkeley.edu)

This work was supported in part by the Intel Corporation via Semiconductor Research Corporation under Grant 2014-IN-2571, in part by the Cambridge Display Technology Limited under Grant 02672530, and in part by the FlexTech under Grant AFOSR-42299.

ABSTRACT Recent progress in printed optoelectronics and their integration in wearable sensors have created new avenues for research in reflectance photoplethysmography (PPG) and oximetry. The reflection-mode sensor, which consists of light emitters and detectors, is a vital component of reflectance oximeters. Here, we report a systematic study of the reflectance oximeter sensor design in terms of component geometry, light emitter and detector spacing, and the use of an optical barrier between the emitter and the detector to maximize sensor performance. Printed red and near-infrared (NIR) organic light-emitting diodes (OLEDs) and organic photodiodes (OPDs) are used to design three sensor geometries: (1) Rectangular geometry, where square OLEDs are placed at each side of the OPD; (2) Bracket geometry, where the OLEDs are shaped as brackets and placed around the square OPD; (3) Circular geometry, where the OLEDs are shaped as block arcs and placed around the circular OPD. Utilizing the bracket geometry, we observe 39.7% and 18.2% improvement in PPG signal magnitude in the red and NIR channels compared to the rectangular geometry, respectively. Using the circular geometry, we observe 48.6% and 9.2% improvements in the red and NIR channels compared to the rectangular geometry. Furthermore, a wearable two-channel PPG sensor is utilized to add redundancy to the measurement. Finally, inverse-variance weighting and template matching algorithms are implemented to improve the detection of heart rate from the multi-channel PPG signals.

INDEX TERMS Reflection photoplethysmography sensor, organic optoelectronics, pulse oximetry, wearable sensors, printed electronics, flexible electronics.

I. INTRODUCTION

In the human body, cardiac rhythm changes the blood volume passing through the arteries, which generates a pulsatile signal that can be optically measured using a light source and a detector; this optical sensing technique is known as photoplethysmography (PPG). Generally, the PPG signal is used for calculating heart rate by utilizing only one light source, and for measuring oxygen saturation (S_pO_2) by employing two light sources. Pulse oximeters measure S_pO_2 of blood by using PPG signals at two distinct wavelengths where light absorption in oxygenated and deoxygenated blood is different [1]. PPG and oximetry can be performed in both transmission and reflection mode. Conventionally, transmission-mode pulse oximeter sensors

composed of solid-state light-emitting diodes (LEDs) and photodiodes (PDs) are used to measure S_pO_2 at the extremities of the body where light can easily penetrate thin regions of tissue, such as the earlobes and the fingertips. However, this method of measuring S_pO_2 presents a few limitations - (i) Transmission-mode oximetry has limited sensing locations [2], and (ii) Solid-state LEDs and PDs do not conform well to the skin, therefore, reduce the signal-to-noise ratio (SNR) [3].

Over the past few years, flexible and wearable sensors are getting significant attention in both academic research and industry due to their skin conformable form factors [4]–[16]. Consequently, flexible optical sensors are extensively studied for PPG and oximetry as they enhance SNR and provide design versatility [2], [3], [17]–[21]. Sensor fabrication and sensing methodology remain a strong focus of recent reports. However, the reflectance oximeter sensor design, which is

The associate editor coordinating the review of this manuscript and approving it for publication was Qingxue Zhang.

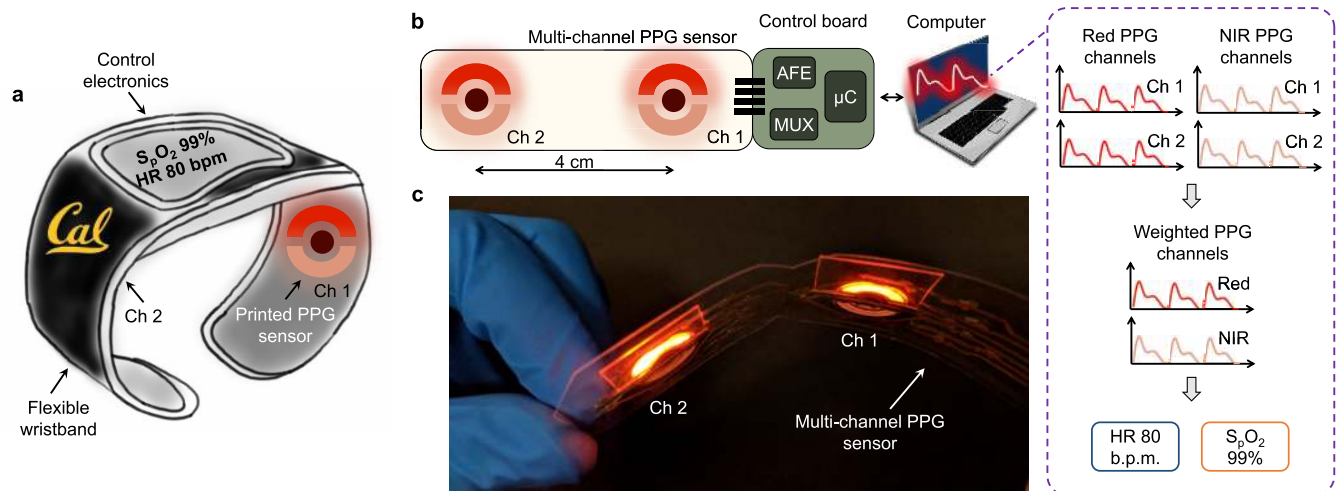


FIGURE 1. Multi-channel reflectance PPG sensor overview. (a) Schematic illustration of a wearable two-channel PPG sensor, where the PPG sensor pixels are mounted on the wristband. (b) Setup for the multi-channel PPG sensor. Two circular sensors are spaced 4 cm apart to collect data from the ulnar artery (Ch 1) and the radial artery (Ch 2). The sensor pixels are driven using an AFE, while multiplexers are used to switch between the pixels. Both red and NIR PPG signals are collected and processed for extracting HR and pulse oxygenation data. (c) Photograph of the multi-pixel reflectance PPG sensor bent to a radius of curvature of 5 cm.

a crucial component of reflection-mode PPG and oximetry, is not well-reported in the literature. In addition, wearable reflection-mode PPG sensors and oximeters are prone to different kinds of noises, such as motion artifacts (MAs), thermal noise, and electromagnetic interference [22]. Thermal noise and electromagnetic interference are high-frequency noise and can be eliminated through filtering. MA, however, is challenging to remove from the PPG signals. Adaptive filtering [23]–[25] and comparing PPG signal to a reference accelerometer signal [25], [26] are popular techniques for reducing MAs. Furthermore, multi-channel PPG signals can also be utilized to extract heart rate and oxygenation information from channels that are less affected by MAs [27], [28]. The multi-channel PPG approach does not require additional hardware blocks or a reference signal.

In this work, we systematically study the reflectance oximeter sensor design in terms of device geometry, light emitter and detector spacing, and the use of an optical barrier between the emitter and the detector to maximize sensor performance. Additionally, we utilize a printed, flexible, and two-channel reflectance oximeter to collect PPG signals using red and near-infrared (NIR) organic light-emitting diodes (OLEDs) and organic photodiodes (OPDs). We implement inverse-variance weighting and template matching algorithms to improve the detection of heart rate from the multi-channel PPG signals. Overall, we report sensor design, optimization, and implementation of a two-channel organic optoelectronic sensor which is promising for wearable smartwatches and wristbands.

II. RESULTS

A. REFLECTANCE OXIMETER SENSOR GEOMETRIES AND OPERATION

A schematic illustration of a two-channel wrist-worn reflectance PPG sensor is shown in Fig. 1a. The multi-channel

sensor is designed using two circular sensors to collect PPG signals from the radial and the ulnar arteries (Fig. 1b). The sensor is interfaced to multiplexers that switch between the pixels and connects to an analog front end (AFE). The AFE sequentially drives the OLEDs and reads out the OPD signals. Since the focus of this article is sensor design and optimization, we use a wired interface for data collection. However, the AFE can be interfaced with a wireless transceiver for wearable applications. Both red and NIR PPG signals are collected using the two pixels. Since most wearable PPG sensors are wrist-worn, we utilize the two-channel PPG sensor for on-wrist measurements. The underside of the wrist, especially on the radial and ulnar arteries, provide the best PPG signal magnitudes. One pixel (Ch 1) is placed on the ulnar artery, while the other pixel (Ch 2) is placed on the radial artery. A photograph of the multi-pixel sensor is shown in Fig. 1c, where the sensor is bent to a radius of curvature of 5 cm to resemble bending on the wrist.

Reflection-mode sensors require light emitters and detectors assembled on a substrate or a circuit board. Traditionally, red and NIR LEDs are placed on either side of the PD to assemble the sensor. The designs of commercially available optoelectronic sensors are limited in shape - typically rectangular, which do not provide much versatility to vary the sensor geometry. On the other hand, printed optoelectronics can be fabricated in various shapes and sizes [29]. In this work, we explore three different sensor geometries as shown in Fig. 2a-c: (1) Rectangular geometry (R), where the OLEDs are placed at either side of the OPD; (2) Bracket geometry (B), where the OLEDs are shaped as brackets and placed around the square OPD; (3) Circular geometry (C), where the OLEDs are shaped as block arcs and placed around the circular OPD. The rectangular sensor design is chosen to represent conventional sensors that use side-by-side optoelectronics placement. The bracket and the circular sensor

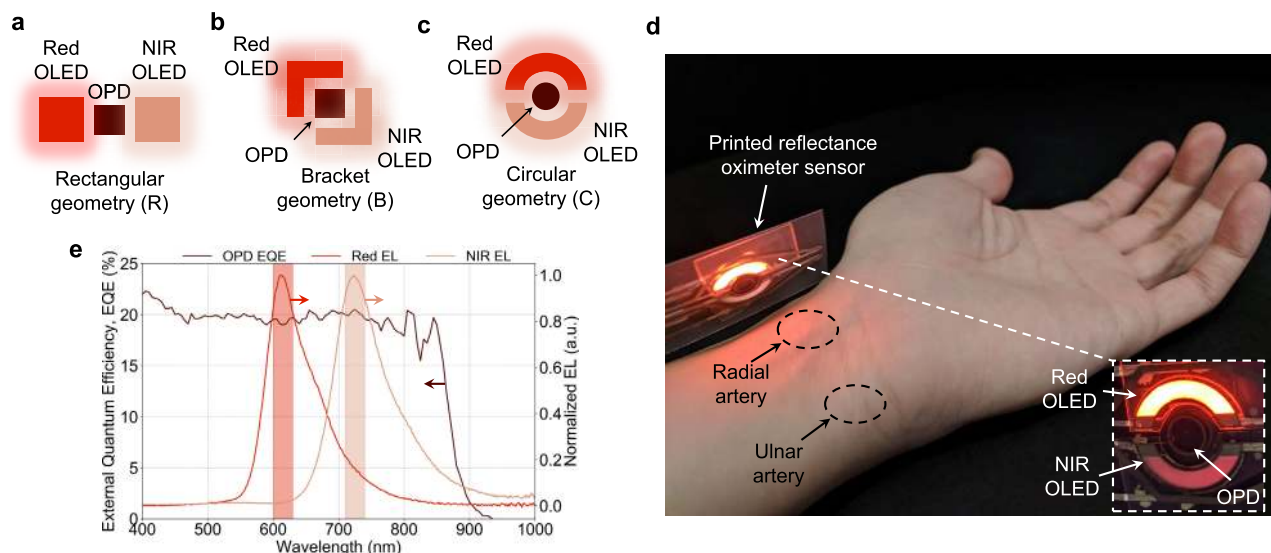


FIGURE 2. Reflectance PPG sensor design and placement on the wrist. (a-c) Different sensor geometries with the same active areas.

(a) Rectangular geometry (R), where the OLEDs are placed at either side of the OPD. (b) Bracket geometry (B), where the OLEDs are shaped as brackets and placed around the square OPD. (c) Circular geometry (C), where the OLEDs are shaped as block arcs and placed around the circular OPD. (d) Photograph of the printed reflectance oximeter sensor placed on the underside of the wrist. The radial and ulnar artery sensing locations are marked to show sensor placement locations. The inset shows a circular sensor with red and NIR OLEDs on the top and the bottom side of the OPD, respectively. (e) Normalized electroluminescence (EL) of the red (red line) and NIR (peach line) OLEDs and EQE of the OPD (brick line). The OPD shows similar EQE at both red and NIR wavelengths.

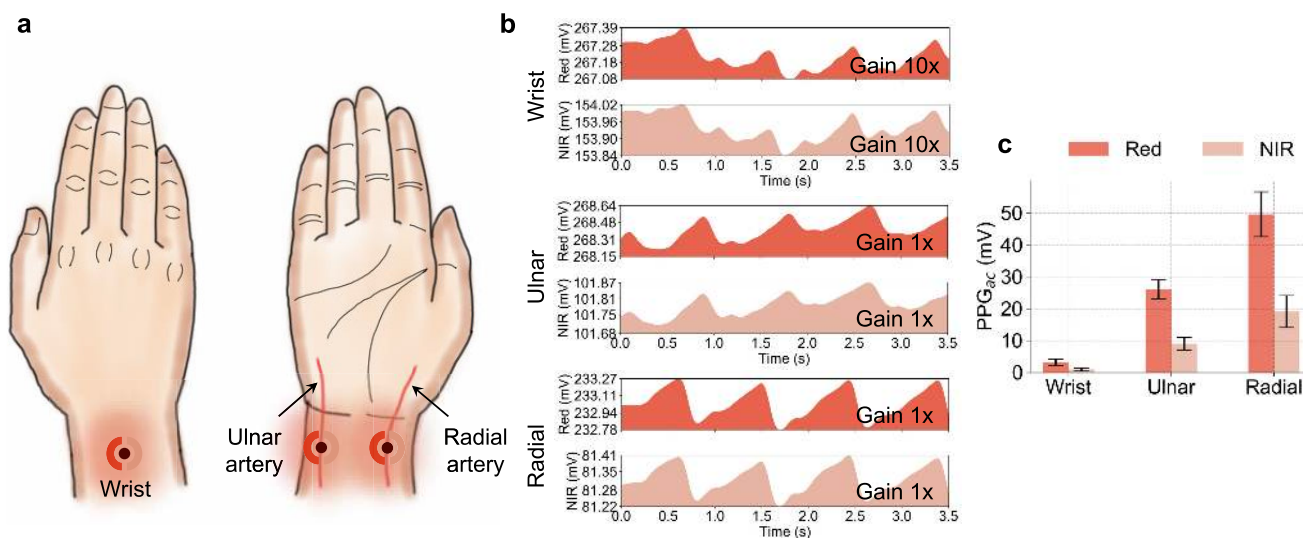


FIGURE 3. PPG signal variation on the wrist. (a) Three sensor placement locations are shown - (i) On top of the wrist, (ii) on top of the ulnar artery, and (iii) on top of the radial artery. (b) PPG signals from the wrist, ulnar and radial arteries are shown. Red color for the red channels and peach color for the NIR channels. Since the signal on the wrist is weak, a 10x gain setting is used to resolve the pulsatile PPG signal. (c) PPG signal magnitudes at the wrist, ulnar and radial arteries. The error bars represent data from 3 separate trials.

geometries are non-traditional geometries chosen to improve PPG SNR. Fig. 2d shows the sensor placement on the underside of the arm. Radial and ulnar arteries are marked to show sensor placement. All sensors are composed of printed red and NIR OLEDs with emission peaks at 630 and 725 nm respectively, and OPDs with external quantum efficiency (EQE) of $\sim 20\%$ at the aforementioned wavelengths (Fig. 2e).

PPG signal magnitudes vary appreciably based on the sensor placement locations on the wrist. We explored three sensing locations: (i) On top of the wrist, (ii) on top of the ulnar artery, and (iii) on top of the radial artery and recorded PPG signals (Fig. 3a and b). While the radial artery provided the cleanest signal (49.50 mV for red and 19.08 mV for NIR), the pulsatile PPG signal on top of the wrist was the weakest

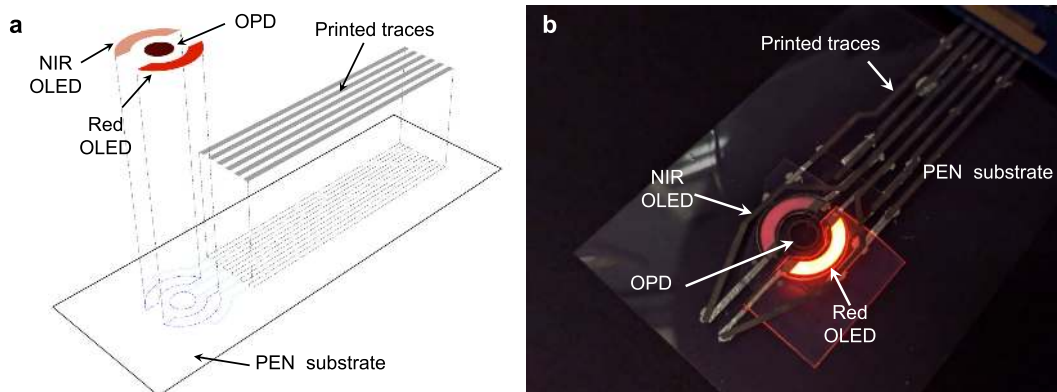


FIGURE 4. Assembly of the printed sensor. (a) Schematic depicting the sensor assembly. Polyethylene naphthalate is used as the base substrate. Inkjet-printed silver traces are used to connect the optoelectronic sensor to the control electronics. Red and NIR OLEDs and the OPD are then connected to complete the sensor. (b) Photograph of the assembled sensor.

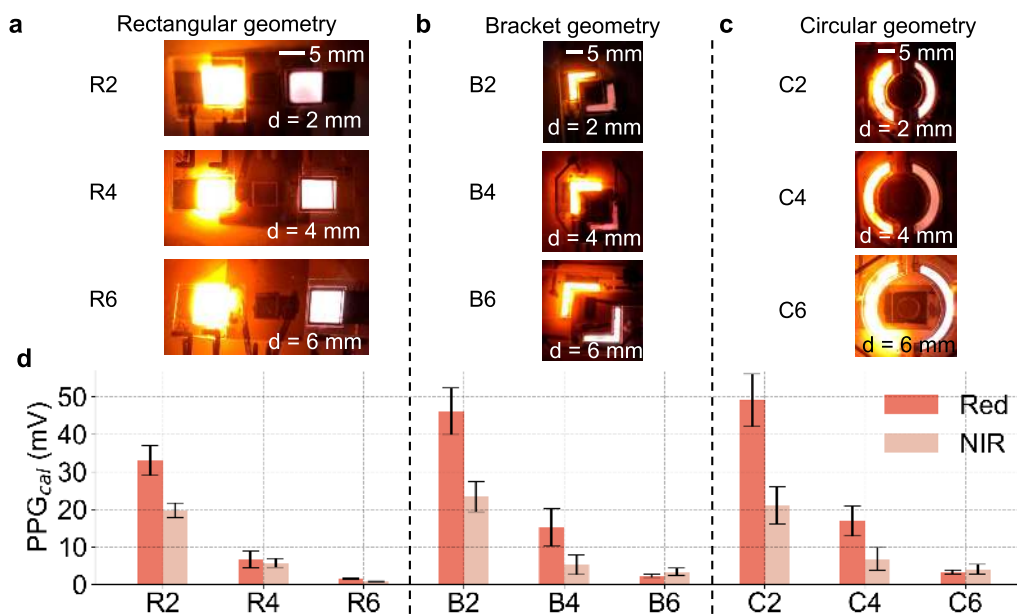


FIGURE 5. Pulsatile signal magnitudes for different sensor geometries. (a) Photographs of the rectangular sensors with emitter-detector spacing, $d = 2, 4, 6$ mm. The devices are labeled as R2, R4, and R6. (b-c) Similar to a, photographs of the bracket and circular sensors with emitter-detector spacing, $d = 2, 4, 6$ mm. The devices are labeled as B2, B4, B6, C2, C4, and C6. (d) The pulsatile signal magnitudes for all rectangular, bracket and circular sensors. Red-colored bars represent data for the red channel, while the peach-colored bars represent data from NIR channel. The error bars represent data from 3 separate trials.

(Fig. 3c). At the ulnar artery an order of magnitude improvement (26.12 mV for red and 9.02 mV for NIR) in PPG signal is observed over the wrist (3.24 mV for red and 0.94 mV for NIR). Therefore, we used our sensor on the underside of the wrist for both single and multi-channel measurements.

B. SENSOR ASSEMBLY AND CALIBRATION

A base polyethylene naphthalate (PEN) substrate is used to assemble the reflectance sensor. Inkjet-printed silver traces are used to route connections from the optoelectronics to the control electronics that consists of an AFE and a micro-controller with a universal serial bus (USB) interface to a computer. The OLEDs and the OPD are printed on separate

plastic substrates and then assembled on the PEN substrate with silver traces as shown in Fig. 4a. The photograph of the assembled sensor with the OLEDs and the OPD is shown in Fig. 4b. Since we are comparing different sensor geometries, a two-step calibration is used to account for the batch-to-batch device variability of the OLEDs and the OPDs. A calibration platform composed of a silicon photodiode and a red LED is used to calibrate the assembled sensor. In the first step, the OLEDs are calibrated using the silicon photodiode by operating the OLEDs at a fixed current and recording the photodiode current. The OLEDs of the assembled sensor are turned on sequentially to measure their intensities using the silicon photodiode. Each OLED is then

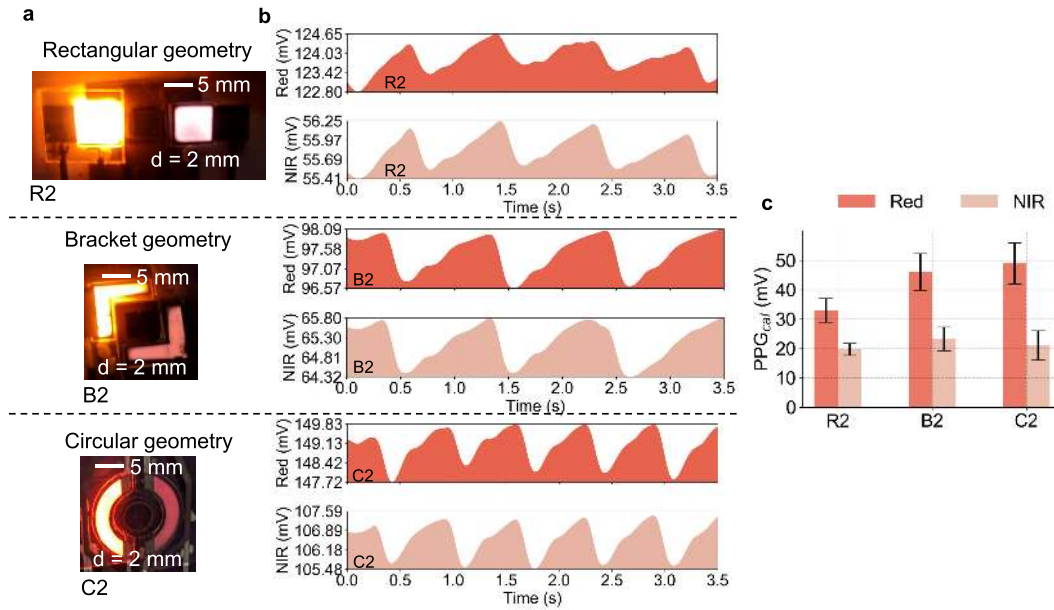


FIGURE 6. Performance comparison of different sensor geometries. (a) Photographs of the rectangular, bracket and circular sensors with an emitter-detector spacing of 2 mm. (b) PPG signals from the red and NIR channels for the sensors shown in (a). (c) The pulsatile signal magnitudes for the smallest rectangular, bracket and circular sensors. Red-colored bars represent data for the red channel, while the peach-colored bars represent data from NIR channel. The error bars represent data from 3 separate trials.

calibrated to the maximum current measured in a batch of devices, $\kappa_{OLED} = \frac{\max(I_{SPD})}{I_{SPD}}$. In the second step, the OPDs are calibrated by recording the OPD current while running the solid-state red LED at a fixed drive current. The red LED of the calibration platform is turned on and the OLEDs are turned off for calibrating the OPDs. The fabricated OPD detects light from the red LED and the measured photocurrent is recorded. Similar to the OLEDs, each OPD is then calibrated to the maximum OPD current measured in a batch of devices, $\kappa_{OPD} = \frac{\max(I_{OPD})}{I_{OPD}}$. The obtained values are then used together with the measured PPG signal to calculate the calibrated signal magnitude. The calibration equation is given below, which is used to compare sensor performances for the three different geometries.

$$PPG_{cal} = \kappa_{OLED} \cdot \kappa_{OPD} \cdot PPG_{meas} [mV] \quad (1)$$

C. PERFORMANCE COMPARISON AMONG DIFFERENT SENSOR GEOMETRIES

After the calibration step, a fair comparison among the three different geometries can be performed. Additionally, we evaluate another important design parameter, emitter-detector spacing, d . Fig. 5a-c show the photographs of the rectangular, bracket, and circular sensors with an emitter-detector spacing of 2, 4, and 6 mm, which are labeled as R2, R4, R6, B2, B4, B6, C2, C4, and C6. These labels are used in Fig. 5d to show pulsatile PPG signal magnitude, PPG_{cal} based on (1).

The rectangular sensor consists of OLEDs and an OPD that are all square-shaped which are placed side-by-side. Since the OLEDs do not surround OPD from the top and the bottom, this scheme is susceptible to ambient light, which contributes

to the noise of the measurement. Also, a significant amount of light coming out from the left edge of the red OLED and the right edge of the NIR OLED do not contribute to the measurement, hence, gets lost. Ideally, a perimeter light source that surrounds the OPD would be the best. The two new schemes, the bracket, and the circular designs, where the light sources encompass the perimeter of the OPD enhance measurement SNR. As shown in Fig. 5d, all three designs show an exponential decay with increasing d . Due to the perimeter lighting and better light collection by the OPD, both bracket and circular geometries outperform the rectangular design in terms of pulsatile PPG signal magnitude. While comparing the bracket and circular design, we observe a negligible difference in PPG_{cal} .

For a direct comparison of the different geometries, we kept the emitter-detector spacing constant at 2 mm, and kept the device area of the OLEDs and the OPDs same for all three geometries as shown in Fig. 6a. The OPD areas are kept fixed at 16 mm^2 and the OLED areas are kept fixed at 28 mm^2 . The PPG waveforms for the different geometries are shown in Fig. 6b. Utilizing the bracket geometry, we observe 39.7% and 18.2% improvements in PPG signal magnitude in the red and NIR channels, respectively over the rectangular geometry. For the circular geometry, we observe 48.6% and 9.2% improvements in the red and NIR channels, respectively over the rectangular geometry. The bracket and the circular design show similar performance in the PPG_{cal} (Fig. 6c). Additionally, the two new designs bring down the overall length of the sensor from 18.6 mm for the rectangular geometry to 12 mm for the bracket and 13.2 mm for the circular geometry.

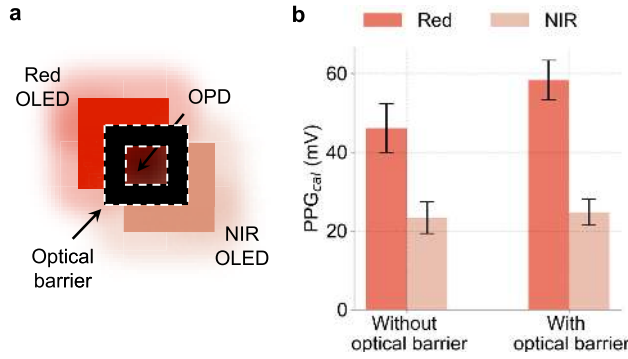


FIGURE 7. The effect of an optical barrier in sensor performance. (a) Schematic of a reflectance oximeter sensor, where an optical barrier is placed in between the emitters and the detector. (b) The pulsatile signal magnitudes of the red and NIR channels without and with the optical barrier. The error bars represent data from 3 separate trials.

In reflectance PPG and oximetry, the light coming back from the arteries contributes to the signal, while the light scattered from the skin surface contributes to noise. Therefore, blocking the light scattered from the skin surface enhances SNR. We incorporated the light blocking feature in our design by utilizing an optical barrier between the OLEDs and OPD. Black tape is cut into the shape that fits the area between the OLEDs and the OPD and is used to block scattered light. Fig. 7a shows the schematic of the sensor. With the blocking layer, we observe 26.5 % improvement in PPG_{cal} in the red channel, and while PPG_{cal} remained almost the same in NIR. Red light scatters more on the skin surface than the NIR. Therefore, more red light scattered by skin surface gets blocked by the optical barrier, resulting in an improved red PPG_{cal} (Fig. 7b).

D. MULTI-CHANNEL PPG SENSOR OPERATION AND DATA PROCESSING

Wearable PPG sensors are susceptible to thermal noise, electromagnetic interference, and MAs. While thermal noise and electromagnetic interference can be reduced with filtering, reducing MAs requires additional hardware and software processing. Adaptive filtering is a popular technique for addressing MAs in PPG signals [23]–[25]. Another approach is to simultaneously record PPG and a reference signal such as an accelerometer signal and apply hybrid algorithms to determine heart rate (HR) and pulse oxygenation [25], [26]. Multi-channel PPG acquisition and processing can also be used to reduce MA by utilizing channels that are lightly influenced by MA [27], [28]. Multiple PPG channels add redundancy to the measurement for signal quality assessment, which is vital for properly extracting HR and pulse oxygenation values. To process multi-channel data, we implemented two algorithms: (1) Template matching (TM) with an ideal PPG signal, and (2) Inverse-variance weighting (IVW). The efficacy of both methods in acquiring high-quality PPG signal, and extracting HR are examined. The process flow of the template matching and inverse-variance weighting algorithms are shown in Fig. 8a and b, respectively.

Both TM and IVW algorithms are used to obtain a weighted PPG signal from multi-channel PPG. The equation for obtaining the weighted PPG is given in (2).

$$PPG_w = \frac{W_1 \times PPG_1 + W_2 \times PPG_2 + \dots + W_n \times PPG_n}{W_1 + W_2 + \dots + W_n} \quad (2)$$

Here, PPG_w is the weighted PPG from all channels, W_i is the weight for channel i determined by either of the two methods discussed in following subsections and PPG_i is the PPG signal from channel i .

E. TEMPLATE MATCHING (TM) WITH AN IDEAL PPG SIGNAL

Template matching is a popular data processing techniques in biomedical signal processing. TM has been widely used in processing electroencephalography (EEG), electrocardiography (ECG), and PPG data [30]–[32]. We use an ideal PPG template to determine the fidelity of the signal from each channel. The ideal template can be obtained from experimental data [33] or by modeling [34]. A small window is acquired from each channel after filtering. Then, troughs are detected to find the pulses in each window. Next, the correlation coefficient of each pulse with the ideal template is calculated. If the correlation coefficient is positive, the correlation coefficient is used as a weight to calculate the weighted average of the two signals. If the correlation coefficient for a pulse is negative, the pulse is ignored, i.e., the weight for that pulse in that channel is set to zero. Thus, using this method, the weight W_i 's in (2) can be given by (3).

$$W_i = \rho_i, \quad \text{if } \rho_i \geq 0, \\ = 0, \quad \text{if } \rho_i < 0 \quad (3)$$

Here, ρ_i is the correlation coefficient between a pulse in channel i and the PPG template. HR and oxygenation values are determined from the weighted signal. The process flow for TM is presented in Fig. 8a.

F. INVERSE-VARIANCE WEIGHTING (IVW) BASED ON HEART RATE

In inverse-variance weighting algorithm, W_i , weight for channel i in (2) are assigned based on the standard deviation of heart rate variability in a specific time window. First, peaks and troughs of the signal from each window are determined. Then, the HR is calculated from the distances in between peaks or troughs. The channel with higher standard deviation in HR is assigned a lower weight, because, in a small time-window of PPG signal, HR should not change too drastically. The weight assignment, in this case, is described by (4).

$$W_i = \frac{1}{\sigma_i} \quad (4)$$

Here, σ_i is the standard deviation of HR in channel i . After assigning the weight, the weighted average of the signals (PPG_w) is computed and the HR and other features are extracted from the signal. The process flow is presented in Fig. 8b.

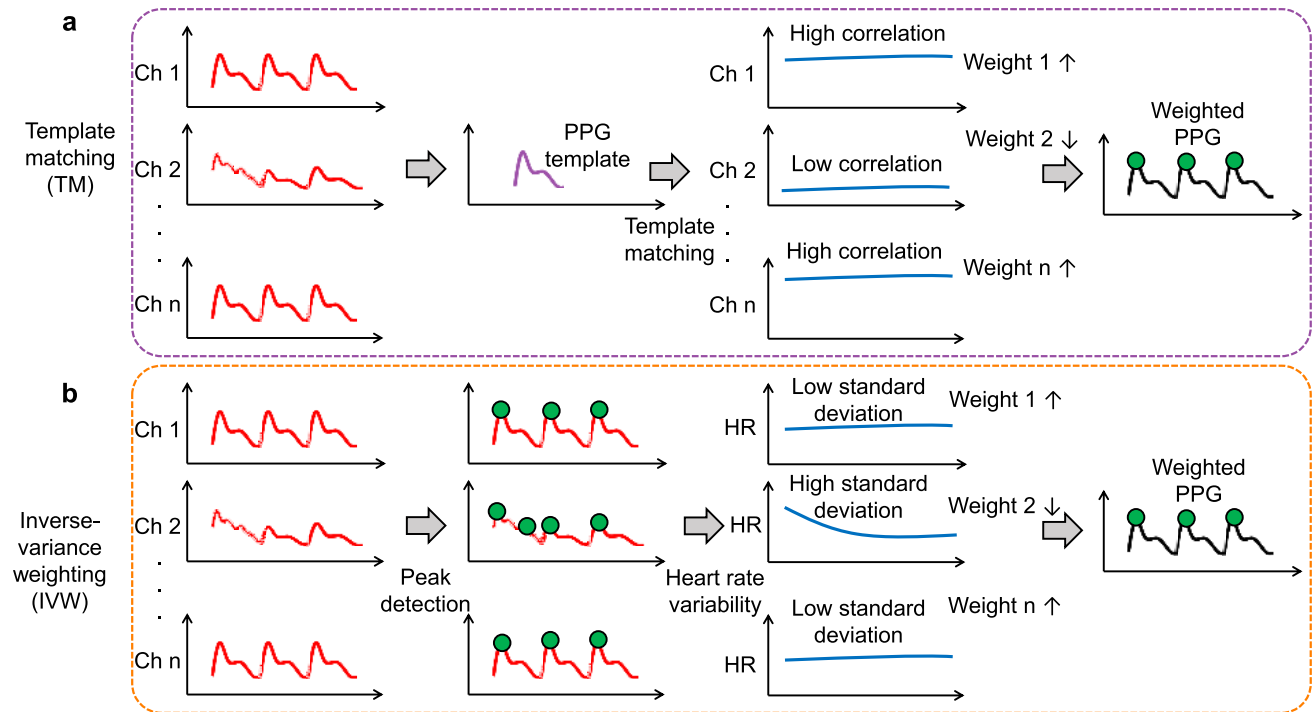


FIGURE 8. Process flow of the (a) Template matching (TM) and (b) Inverse-variance weighting (IVW) algorithms.

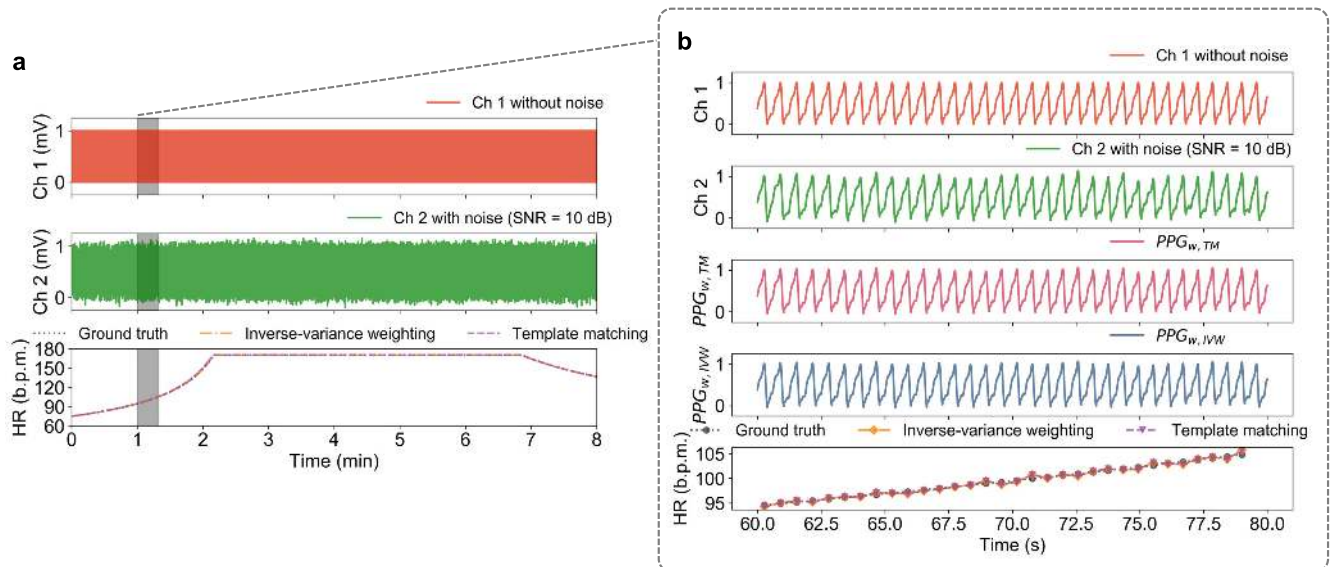


FIGURE 9. Heart rate detection using TM and IVW algorithms from a simulated dataset. (a) 8 min long pristine PPG signal (Ch 1, top panel) and a PPG signal with 10 dB SNR (Ch 2, middle panel) are used as the multi-channel PPG data. Calculated HR from Ch 1 and Ch 2 using TM and IVW algorithms and the ground truth are shown in the bottom panel. (b) Zoomed-in data from 60 to 80 s of a - Ch 1, Ch 2, weighted PPG signal using TM and IVW algorithms, and calculated HR are shown.

G. IMPLEMENTATION OF TM AND IVW ALGORITHMS ON A SIMULATED PPG DATASET

To test the efficacy of the TM and IVW algorithms, a simulated dataset is used to determine HR variability over time. The simulated dataset is designed to represent HR variability while performing an exercise (Fig. 9a). Here, Ch 1 is a

simulated PPG signal, where the HR goes up in the first few minutes, stays constant and then goes down slowly. This PPG signal represents the change in PPG during real-time exercise. Ch 2 is the same PPG signal with a low-frequency noise added to it. Slow and fast variations of HR are utilized. In the fast variation case, HR is varied from 71 beats per min (b.p.m.)

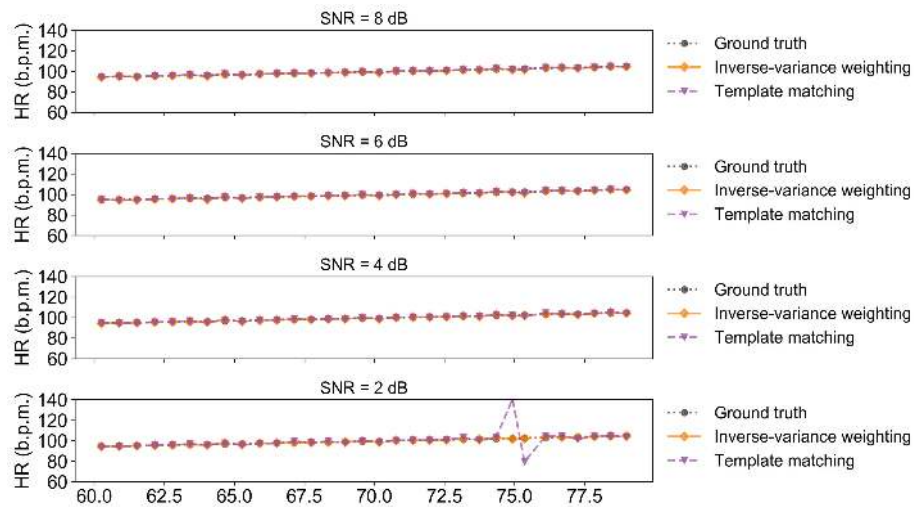


FIGURE 10. The effect of SNR on the accuracy of HR estimation using TM and IVW algorithms.

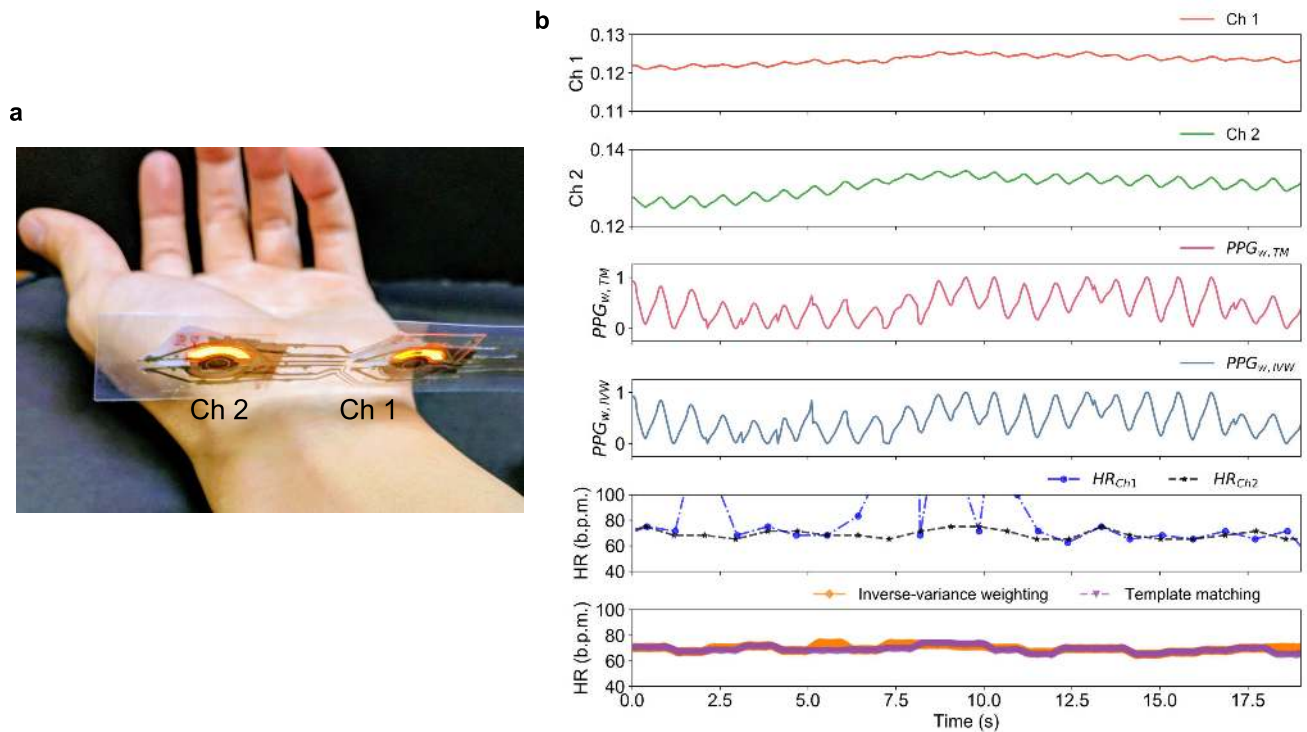


FIGURE 11. Heart rate detection using TM and IVW algorithms from the printed multi-channel PPG sensor. (a) The printed sensor is placed on the underside of the wrist. (b) Ch 1 and Ch 2 are PPG data collected from the ulnar and the radial arteries, respectively. $PPG_{w, TM}$ and $PPG_{w, IVW}$ are the weighed PPG signals generated by TM and IVW algorithms. HR_{Ch1} and HR_{Ch2} are calculated heart rate by using Ch 1 and Ch 2 PPG data. The bottom panel shows calculated HR by TM and IVW algorithms.

to 200 b.p.m. in 20 s. Both TM and IVW algorithms successfully reconstructed the PPG signals and determine HR accurately. In the slow variation case, HR was varied from 95 to 105 b.p.m. in 20 s (Fig. 9b), and both the algorithms successfully determined HR in this test case also.

The effect of noise on the accuracy of determining HR using TM and IVW algorithms is examined by adding noise

of frequency below 5 Hz to one of the channels. This frequency range of noise is chosen because noise with a frequency above 5 Hz can be removed from the signal using a low-pass filter (LPF). The effect of SNR is shown in Fig. 10. The SNR is varied and as long as the SNR is above 3 dB, both algorithms accurately detect HR. However, at SNR less than 3 dB, the TM algorithm fails to predict HR accurately.

TABLE 1. Heart rate calculated from a literature dataset [25] using template matching and inverse-variance weighting algorithms.

Dataset	Template Matching	Inverse-Variance Weighting	Ground Truth
I	74.26	74.26	74.34
II	64.66	64.66	68.73
III	72.12	72.12	74.53

In addition to the simulated dataset, we used three sets of PPG dual-channel data reported by Zhang *et al.* [25] to test the efficacy of the TM and IVW algorithms. The results are summarized in Table 1. For the datasets, I and III the HR calculated using both methods are close to the ground truth HR, i.e., within 2 b.p.m. However, in dataset II, both channels are severely affected by MA, so the calculated HRs are further away from ground truth HR. For accurate detection of HR, at least one of the channels should be minimally affected by MA so that the PPG pulses are recognizable.

H. IMPLEMENTATION OF TM AND IVW ALGORITHMS ON THE PRINTED MULTI-CHANNEL PPG SENSOR DATA

After validating the TM and IVW algorithms on the simulated and literature datasets, we employed both methods for processing the data collected by the printed multi-channel PPG sensor. The sensor is placed on the underside of the wrist, where Ch 1 collects data from the ulnar artery and Ch 2 collects data from the radial artery (Fig. 11a and b, top two panels). The weighed PPG signals generated by TM and IVW algorithms are shown in panel 3 and 4 of Fig. 11b. Here, the signal magnitude of Ch 1 is weaker compared to Ch 2. Therefore, HR calculated using only using Ch 1 PPG signal demonstrates significant variation (panel 5 of Fig. 11b). After implementing TM and IVW algorithms, accurate detection of HR is observed for both the algorithms (bottom panel of Fig. 11b), demonstrating the feasibility of using these two methods for wearable PPG sensors and oximeters.

III. DISCUSSION

By utilizing the versatility of printed electronics, optoelectronic sensors for PPG and oximetry are fabricated in different shapes and sizes. In this work, we utilized non-conventional geometries such as bracket and circular designs to improve sensor performance. The new sensor geometries demonstrated a clear improvement over the conventional rectangular sensor design. Moreover, we used a wearable two-channel PPG sensor to add redundancy to the measurement and demonstrated the effectiveness of inverse-variance weighting and template matching algorithms to improve the detection of heart rate from the multi-channel PPG signals. The new sensor geometries not only improved the PPG signal magnitudes but also decreased the overall sensor length and reduced power consumption. These sensor designs coupled with multi-channel redundancy can be incorporated into

wrist-worn devices, making them extremely promising for wearable reflectance PPG and oximetry.

ACKNOWLEDGMENT

The authors thank David Rosales, Claire Lochner, Gianluca Bovo, Nir Yaacobi-Gross, Chris Newsome, Richard Wilson, and Sifat Muin for helpful technical discussions. *Yasser Khan, Donggeon Han, Jonathan Ting, and Maruf Ahmed contributed equally to this work.*

REFERENCES

- [1] J. G. Webster, *Design of Pulse Oximeters*. Boca Raton, FL, USA: CRC Press, 1997.
- [2] Y. Khan, D. Han, A. Pierre, J. Ting, X. Wang, C. M. Lochner, G. Bovo, N. Yaacobi-Gross, C. Newsome, R. Wilson, and A. C. Arias, "A flexible organic reflectance oximeter array," *Proc. Nat. Acad. Sci. USA*, vol. 115, no. 47, pp. E11015–E11024, 2018.
- [3] C. M. Lochner, Y. Khan, A. Pierre, and A. C. Arias, "All-organic optoelectronic sensor for pulse oximetry," *Nature Commun.*, vol. 5, p. 5745, Dec. 2014.
- [4] T. Q. Trung and N.-E. Lee, "Flexible and stretchable physical sensor integrated platforms for wearable human-activity monitoring and personal healthcare," *Adv. Mater.*, vol. 28, no. 22, pp. 4338–4372, 2016.
- [5] S. Choi, H. Lee, R. Ghaffari, T. Hyeon, and D.-H. Kim, "Recent advances in flexible and stretchable bio-electronic devices integrated with nanomaterials," *Adv. Mater.*, vol. 28, no. 22, pp. 4203–4218, 2016.
- [6] T. Someya, Z. Bao, and G. G. Malliaras, "The rise of plastic bioelectronics," *Nature*, vol. 540, pp. 379–385, Dec. 2016.
- [7] M. Poliks, J. Turner, K. Ghose, Z. Jin, M. Garg, Q. Gui, A. Arias, Y. Kahn, M. Schadt, and F. Egitto, "A wearable flexible hybrid electronics ECG monitor," in *Proc. IEEE 66th Electron. Compon. Technol. Conf. (ECTC)*, May/Jun. 2016, pp. 1623–1631.
- [8] V. Soman, Y. Khan, M. Zabran, M. Schadt, P. Hart, M. Shay, F. Egitto, K. Papathomas, N. A. D. Yamamoto, D. Han, A. C. Arias, K. Ghose, M. D. Poliks, J. N. Turner, "Reliability challenges in fabrication of flexible hybrid electronics for human performance monitors: A system level study," *IEEE Trans. Compon., Packag. Manuf. Technol.*, to be published.
- [9] S. Jung, S. Hong, J. Kim, S. Lee, T. Hyeon, M. Lee, and D.-H. Kim, "Wearable fall detector using integrated sensors and energy devices," *Sci. Rep.*, vol. 5, Nov. 2015, Art. no. 17081.
- [10] S. Choi, S. I. Han, D. Jung, H. J. Hwang, C. Lim, S. Bae, O. K. Park, C. M. Tschabrunn, M. Lee, S. Y. Bae, J. W. Yu, J. H. Ryu, S.-W. Lee, K. Park, P. M. Kang, W. B. Lee, R. Nezafat, T. Hyeon, and D.-H. Kim, "Highly conductive, stretchable and biocompatible Ag–Au core–sheath nanowire composite for wearable and implantable bioelectronics," *Nature Nanotechnol.*, vol. 13, pp. 1048–1056, 2018.
- [11] M. F. Farooqui and A. Shamim, "Low cost inkjet printed smart bandage for wireless monitoring of chronic wounds," *Sci. Rep.*, vol. 6, Jun. 2016, Art. no. 28949.
- [12] J. M. Nassar, K. Mishra, K. Lau, A. A. Aguirre-Pablo, and M. M. Hussain, "Recyclable nonfunctionalized paper-based ultralow-cost wearable health monitoring system," *Adv. Mater. Technol.*, vol. 2, no. 4, 2017, Art. no. 1600228.
- [13] L. Engel, C. Liu, N. M. Hemed, Y. Khan, A. C. Arias, Y. Shacham-Diamand, S. Krylov, and L. Lin, "Local electrochemical control of hydrogel microactuators in microfluidics," *J. Microelectromech. Microeng.*, vol. 28, no. 10, 2018, Art. no. 105005.
- [14] A. Moin, A. Zhou, A. Rahimi, S. Benatti, A. Menon, S. Tamakloe, J. Ting, N. Yamamoto, Y. Khan, F. Burghardt, L. Benini, A. C. Arias, and J. M. Rabaey, "An EMG gesture recognition system with flexible high-density sensors and brain-inspired high-dimensional classifier," in *Proc. IEEE Int. Symp. Circuits Syst. (ISCAS)*, May 2018, pp. 1–5.
- [15] A. E. Ostfeld, A. M. Gaikwad, Y. Khan, and A. C. Arias, "High-performance flexible energy storage and harvesting system for wearable electronics," *Sci. Rep.*, vol. 6, May 2016, Art. no. 26122.
- [16] A. Thielens, I. Deckman, R. Aminzadeh, A. C. Arias, and J. M. Rabaey, "Fabrication and characterization of flexible spray-coated antennas," *IEEE Access*, vol. 6, pp. 62050–62061, 2018.

- [17] T. Yokota, P. Zalar, M. Kaltenbrunner, H. Jinno, N. Matsuhisa, H. Kitano, Y. Tachibana, W. Yukita, M. Koizumi, and T. Someya, "Ultraflexible organic photonic skin," *Sci. Adv.*, vol. 2, no. 4, Apr. 2016, Art. no. e1501856.
- [18] J. Kim *et al.*, "Battery-free, stretchable optoelectronic systems for wireless optical characterization of the skin," *Sci. Adv.*, vol. 2, no. 8, 2016, Art. no. e1600418.
- [19] D. Han, Y. Khan, J. Ting, S. M. King, N. Yaacobi-Gross, M. J. Humphries, C. J. Newsome, and A. C. Arias, "Flexible blade-coated multicolor polymer light-emitting diodes for optoelectronic sensors," *Adv. Mater.*, vol. 29, no. 22, Jun. 2017, Art. no. 1606206.
- [20] D. Yin, N.-R. Jiang, Y.-F. Liu, X.-L. Zhang, A.-W. Li, J. Feng, and H.-B. Sun, "Mechanically robust stretchable organic optoelectronic devices built using a simple and universal stencil-pattern transferring technology," *Light, Sci. Appl.*, vol. 7, no. 1, 2018, Art. no. 35.
- [21] H. Lee, E. Kim, Y. Lee, H. Kim, J. Lee, M. Kim, H.-J. Yoo, and S. Yoo, "Toward all-day wearable health monitoring: An ultralow-power, reflective organic pulse oximetry sensing patch," *Sci. Adv.*, vol. 4, no. 11, 2018, Art. no. eaas9530.
- [22] M. R. Ram, K. V. Madhav, E. H. Krishna, N. R. Komalla, and K. A. Reddy, "A novel approach for motion artifact reduction in PPG signals based on AS-LMS adaptive filter," *IEEE Trans. Instrum. Meas.*, vol. 61, no. 5, pp. 1445–1457, May 2012.
- [23] F. Peng, Z. Zhang, X. Gou, H. Liu, and W. Wang, "Motion artifact removal from photoplethysmographic signals by combining temporally constrained independent component analysis and adaptive filter," *Biomed. Eng. OnLine*, vol. 13, no. 1, p. 50, 2014.
- [24] H. Han, M.-J. Kim, and J. Kim, "Development of real-time motion artifact reduction algorithm for a wearable photoplethysmography," in *Proc. 29th IEEE Annu. Int. Conf. Eng. Med. Biol. Soc. (EMBS)*, Aug. 2007, pp. 1538–1541.
- [25] Z. Zhang, Z. Pi, and B. Liu, "TROIKA: A general framework for heart rate monitoring using wrist-type photoplethysmographic signals during intensive physical exercise," *IEEE Trans. Biomed. Eng.*, vol. 62, no. 2, pp. 522–531, Feb. 2015.
- [26] Z. Zhang, "Heart rate monitoring from wrist-type photoplethysmographic (PPG) signals during intensive physical exercise," in *Proc. IEEE Global Conf. Signal Inf. Process. (GlobalSIP)*, Dec. 2014, pp. 698–702.
- [27] S.-T. Lin, W.-H. Chen, and Y.-H. Lin, "A pulse rate detection method for mouse application based on multi-PPG sensors," *Sensors*, vol. 17, no. 7, p. 1628, 2017.
- [28] K. M. Warren, J. R. Harvey, K. H. Chon, and Y. Mendelson, "Improving pulse rate measurements during random motion using a wearable multi-channel reflectance photoplethysmograph," *Sensors*, vol. 16, no. 3, p. 342, 2016.
- [29] D. Han, Y. Khan, K. Gopalan, A. Pierre, and A. C. Arias, "Emission area patterning of organic light-emitting diodes (OLEDs) via printed dielectrics," *Adv. Funct. Mater.*, vol. 28, no. 37, 2018, Art. no. 1802986.
- [30] H. Qu and J. Gotman, "A patient-specific algorithm for the detection of seizure onset in long-term EEG monitoring: Possible use as a warning device," *IEEE Trans. Biomed. Eng.*, vol. 44, no. 2, pp. 115–122, Feb. 1997.
- [31] M. Baumert, V. Starc, and A. Porta, "Conventional QT variability measurement vs. template matching techniques: Comparison of performance using simulated and real ECG," *PLoS ONE*, vol. 7, no. 7, 2012, Art. no. e41920.
- [32] C. Orphanidou, T. Bonnici, P. Charlton, D. Clifton, D. Vallance, and L. Tarassenko, "Signal-quality indices for the electrocardiogram and photoplethysmogram: Derivation and applications to wireless monitoring," *IEEE J. Biomed. Health Informat.*, vol. 19, no. 3, pp. 832–838, May 2015.
- [33] Y. Liang, M. Elgendi, Z. Chen, and R. Ward, "An optimal filter for short photoplethysmogram signals," *Sci. Data*, vol. 5, May 2018, Art. no. 180076.
- [34] F. Rundo, S. Conoci, A. Ortis, and S. Battiatto, "An advanced bio-inspired photoplethysmography (PPG) and ECG pattern recognition system for medical assessment," *Sensors*, vol. 18, no. 2, p. 405, Jan. 2018.



YASSER KHAN received the B.S. degree in electrical engineering from The University of Texas at Dallas, in 2010, the M.S. degree in electrical engineering from the King Abdullah University of Science and Technology, in 2012, and the Ph.D. degree in electrical engineering and computer sciences from the University of California, Berkeley, in 2018, from Professor Ana Claudia Arias' research group. He is currently a Postdoctoral Scholar with Stanford University, advised by

Professor Zhenan Bao in chemical engineering and Professor Boris Murmann in electrical engineering. His research interests include wearable medical devices, with an emphasis on skin-like soft sensor systems. His research experience includes internships at Oxford University, Stanford University, and Zyvex Labs in Texas.



DONGGEON HAN received the bachelor's, master's, and Ph.D. degrees from the Korea Advanced Institute of Science and Technology, all in electrical engineering, in 2009, 2011, and 2015, respectively.

He was a Postdoctoral Researcher with the Department of Electrical Engineering and Computer Sciences, University of California, Berkeley, from 2015 to 2018. He conducted research on printed optoelectronic sensors and devices. He is currently a Hardware Engineer with Apple.



JONATHAN TING received the B.S. degree in electrical engineering from the Georgia Institute of Technology, in 2015. He is currently pursuing the Ph.D. degree with the Department of Electrical Engineering and Computer Sciences, University of California, Berkeley, from Professor Ana Claudia Arias' research group. His research interests primarily include flexible wearable sensors, with a focus in printed optoelectronics and biosensors.



MARUF AHMED received the bachelor's and master's degrees in electrical and electronic engineering from the Bangladesh University of Engineering and Technology, in 2013 and 2016, respectively. In undergraduate research, he has investigated the feasibility of quantum cascade structures for thermophotovoltaic energy harvesting application. In his M.Sc. thesis, he has worked on III–V material-based type II quantum well-infrared photodetectors. His current research interests include printed organic photodiodes and phototransistors.



RAMUNE NAGISETTY received the BSEE degree from Northwestern University, in 1991, and the MSEE degree specializing in solid-state physics from the University of California, Berkeley, in 1995.

She joined Intel as a Rotation Engineer, in 1995, and spent the next ten years working on process technology and transistor device physics within the Intel's Logic Technology Development Group. She delivered Intel's first strained silicon technol-

ogy to manufacturing and did pathfinding studies for Hi-K Metal Gate and Tri-gate (FinFET) transistors. From 2006 to 2009, she was the Director of Intel's Strategic Technology Programs, where she worked with technologists and executives to understand opportunities and gaps in Intel's future technology roadmaps. From 2009 to 2017, she led research in systems engineering and prototyping for multidisciplinary projects that involve creating novel usage models and the proofs of concept in three areas: wearable authentication, emotional and social communication, and novel wearable form factors based on printed flexible electronics. Most recently, she led work in using chiplets and package level integration to reduce overall portfolio cost, scale innovation, and speed time to market. She is currently a Senior Principal Engineer and the Director of the Process and Product Integration in Intel's Technology Development Group.



ANA C. ARIAS received the bachelor's and master's degrees from the Federal University of Paraná, Curitiba, Brazil, in 1995 and 1997, respectively, and the Ph.D. degree from the University of Cambridge, U.K., in 2001, all in physics.

She was the Manager of the Printed Electronic Devices Area and a member of Research Staff with PARC, a Xerox Company. She went to PARC, in 2003, from Plastic Logic, Cambridge, U.K., where she led the semiconductor group. She is currently a Professor of electrical engineering and computer sciences with the University of California, Berkeley. Her research interests include the use of electronic materials processed from solution in flexible electronic systems. She uses printing techniques to fabricate flexible large-area electronic devices and sensors.

...